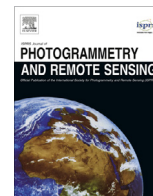




Contents lists available at ScienceDirect

ISPRS Journal of Photogrammetry and Remote Sensing

journal homepage: www.elsevier.com/locate/isprsjprs

Assessing integration of intensity, polarimetric scattering, interferometric coherence and spatial texture metrics in PALSAR-derived land cover classification



Huiran Jin ^{a,*}, Giorgos Mountrakis ^a, Stephen V. Stehman ^b

^a Department of Environmental Resources Engineering, State University of New York College of Environmental Science and Forestry, 1 Forestry Dr., Syracuse, NY 13210, USA

^b Department of Forest and Natural Resources Management, State University of New York College of Environmental Science and Forestry, 1 Forestry Dr., Syracuse, NY 13210, USA

ARTICLE INFO

Article history:

Received 20 March 2014

Received in revised form 6 August 2014

Accepted 30 September 2014

Available online 30 October 2014

Keywords:

ALOS/PALSAR

Dual polarization

Feature synergy

Land cover classification

Stratified sampling

Accuracy assessment

ABSTRACT

Synthetic aperture radar (SAR) is an important alternative to optical remote sensing due to its ability to acquire data regardless of weather conditions and day/night cycle. The Phased Array type L-band SAR (PALSAR) onboard the Advanced Land Observing Satellite (ALOS) provided new opportunities for vegetation and land cover mapping. Most previous studies employing PALSAR investigated the use of one or two feature types (e.g. intensity, coherence); however, little effort has been devoted to assessing the simultaneous integration of multiple types of features. In this study, we bridged this gap by evaluating the potential of using numerous metrics expressing four feature types: intensity, polarimetric scattering, interferometric coherence and spatial texture. Our case study was conducted in Central New York State, USA using multitemporal PALSAR imagery from 2010. The land cover classification implemented an ensemble learning algorithm, namely random forest. Accuracies of each classified map produced from different combinations of features were assessed on a pixel-by-pixel basis using validation data obtained from a stratified random sample. Among the different combinations of feature types evaluated, intensity was the most indispensable because intensity was included in all of the highest accuracy scenarios. However, relative to using only intensity metrics, combining all four feature types increased overall accuracy by 7%. Producer's and user's accuracies of the four vegetation classes improved considerably for the best performing combination of features when compared to classifications using only a single feature type.

© 2014 International Society for Photogrammetry and Remote Sensing, Inc. (ISPRS). Published by Elsevier B.V. All rights reserved.

1. Introduction

Timely land cover information is essential for land resources management and conservation. Satellite remote sensing plays a key role in land cover monitoring due to its ability to obtain up-to-date information over large areas at relatively low cost. In the last few decades, optical satellite imagery has been extensively used to classify land cover (e.g. Hansen et al., 2000; Friedl et al., 2002; Homer et al., 2004, 2007). Nonetheless, the utility of optical data is highly restricted by solar illumination and atmospheric conditions, particularly in regions at high latitudes and/or prone to persistent cloud cover and heavy precipitation.

Synthetic aperture radar (SAR) is an important alternative to optical remote sensing. As an active microwave sensing system,

* Corresponding author at: Department of Geographical Sciences, University of Maryland, College Park, MD 20742, USA. Tel.: +1 315 382 9566.

E-mail addresses: hrjin@umd.edu (H. Jin), gmountrakis@esf.edu (G. Mountrakis), svstehma@syr.edu (S.V. Stehman).

SAR has an inherent advantage over optical sensors for its day-and-night and all-weather observation capability, which guarantees multiple image acquisitions over relatively short periods of time. Moreover, radar signals are sensitive to properties of soil (e.g. moisture and roughness) and vegetation (e.g. structure and biomass) (Fung, 1994; Ulaby et al., 1986), providing complementary characterization of land cover types relative to that achieved with optical imagery (Pohl and van Genderen, 1998).

The investigation of timely land cover information using radar remote sensing has become more practical since spaceborne SAR systems were developed and launched for regular data collection. Major past and current operational SAR sensors are COSMO-SkyMed (X-band), TerraSAR-X (X-band), TanDEM-X (X-band), ERS-1/2 (C-band), Radarsat-1/2 (C-band), Envisat/ASAR (C-band), Sentinel-1A (C-band), Seasat-1 (L-band), JERS-1 (L-band), ALOS/PALSAR (L-band), and ALOS-2/PALSAR-2 (L-band). The letter codes for the various bands correspond to different wavelength ranges, which determine the extent to which a radar signal is attenuated

and/or dispersed by the atmosphere. Although radar signals are barely affected by clouds, the influence of heavy precipitation can be considerable at K- and X-band with operating wavelengths less than 4 cm (Dankmayer et al., 2009). In addition, radar wavelength is directly related to the depth of penetration into the canopy, and this depth determines the contribution of various scattering components to radar backscatter. Short wavelengths such as X-band (2.4–3.75 cm) and C-band (3.75–7.5 cm) mainly interact with the top leaves/needles, twigs and small branches, whereas long wavelengths such as L-band (15–30 cm) and P-band (30–100 cm) penetrate deeper into vegetation canopies and interact mostly with primary branches, tree trunks and also the underlying ground (Ulaby et al., 1986; Le Toan et al., 1992). The penetration depth of radar signals in other targets, such as snow and ice, also varies with the wavelength (Hoen and Zebker, 2000; Rignot et al., 2001).

In January 2006, the Japan Aerospace Exploration Agency (JAXA) successfully launched the Advanced Land Observing Satellite (ALOS). The Phased Array type L-band SAR (PALSAR) onboard the satellite operates in the L-band with 1270-MHz (23.6 cm) center frequency and 14- and 28-MHz bandwidths. It has five different observation modes: Fine Beam Single (FBS) polarization (HH or VV), Fine Beam Dual (FBD) polarization (HH/HV or VV/VH), Polarimetric (PLR) mode (HH/HV/VH/VV), ScanSAR mode, and Direct Transmission (DT) mode, where HH, HV, VH and VV represent the polarizations (horizontal or vertical) of transmitted (first letter) and received (second letter) radar signals. PALSAR data were consistently acquired on a repetitive basis of 46 days at off-nadir looking angles ranging from 9.7 to 50.8 degree, with ground resolutions from 10 to 100 m and swath widths from 30 to 360 km (Rosenqvist et al., 2007). These characteristics, especially the L-band frequency and multi-polarization modes, provide enhanced sensitivity to vegetation responses (Almeida-Filho et al., 2009). Accordingly, PALSAR imagery has been increasingly used in recent studies on vegetation information extraction, for example, crop classification (McNairn et al., 2009), forest cover monitoring (Thiel et al., 2009), forest growth stage investigation (Santoro et al., 2009), and forest species composition mapping (Wolter and Townsend, 2011; Miettinen and Liew, 2011).

Although PALSAR ceased functioning in May 2011 when the ALOS mission was terminated due to a power generation anomaly, it acquired thousands of L-band images during its five year operation, greatly contributing to the fields of cartography, regional land observation, disaster monitoring, and resource survey. Successful applications of PALSAR and its predecessor JERS-1 (the Japanese Earth Resources Satellite-1) (e.g. Simard et al., 2000; Rauste, 2005; Santoro et al., 2006) encourage the development of the follow-on mission ALOS-2 with PALSAR-2 onboard, which was designed to have enhanced performance on spatial resolution and observation frequency compared to ALOS/PALSAR. The ALOS-2 was launched on 24 May 2014, and it is currently under initial function verification. Images acquired by PALSAR-2 are planned to go public in November, 2014 (JAXA, 2014).

2. Background and research objective

Many features can be extracted from PALSAR imagery with the backscattering coefficient among the most commonly used. Expressing the strength (or intensity) of radar signals received by the sensor after scattering, the backscattering coefficient is a fundamental indicator of ground conditions, particularly of vegetation growth, due to its sensitivity to surface roughness with respect to polarization (e.g. Santoro et al., 2010; Dong et al., 2012). Polarimetric decomposition through eigen analysis on the complex data

identifies characteristics that describe the type and contribution of scattering mechanisms, providing a meaningful and thorough exploitation of SAR polarimetry with the inclusion of the phase information that is discarded in studies using backscattering coefficient exclusively (e.g. McNairn et al., 2009). SAR interferometry, which is based on a combination of two complex images acquired at separate times over the target area, can be used to retrieve information complementary to that contained in individual images. Quantifying the degree of similarity, interferometric coherence is close or equal to one for two identical images and close or equal to zero for two completely different images (e.g. Meyer et al., 2011). Furthermore, textural information is considered an important data source for the description of spatial pattern and variation of surface features. Some previous studies have demonstrated the usefulness of texture measures as integrated with intensity data for land cover mapping (e.g. Walker et al., 2010; Longepe et al., 2011).

Table 1 provides a review of current studies using PALSAR-derived features gleaned from five major remote sensing journals: *Remote Sensing of Environment*, *ISPRS Journal of Photogrammetry and Remote Sensing*, *IEEE Transactions on Geoscience and Remote Sensing*, *IEEE Journal of Selected Topics in Applied Earth Observations and Remote Sensing*, and *International Journal of Remote Sensing*. These studies were chosen as they intended to use PALSAR data to monitor land cover resources such as forest and agriculture. Studies on lahar path detection (Joyce et al., 2009), estuarine shoreline delineation (Wang and Allen, 2008), and seismic surface displacement analysis (Zhang et al., 2010) were selectively included to showcase the diversity of PALSAR applications.

The use of different types of features in the sample articles is summarized in Table 1. Intensity was adopted in 22 of the 24 selected studies, where we define “intensity” to represent not only the backscattering coefficient, but also metrics computed based on the backscattering coefficient. For example, in Baghdadi et al. (2009), two polarization bands recording HH and HV backscatters and their difference (HH–HV) were compared with crop height and NDVI to investigate the correlations, respectively. Moreover, Almeida-Filho et al. (2009) defined a Normalized Difference Index (NDI) on HH and HV to enhance the detection of new deforestation areas. Several of these articles employed interferometric coherence when multitemporal PALSAR scenes were available, and the increase of information by the synergistic use of intensity and coherence was examined (e.g. Lonnqvist et al., 2010; Tanase et al., 2010, 2011). In contrast, polarimetric decomposition was employed in only two studies and texture feature extraction was used in three studies. The majority of studies (14 of 24) were based on a single feature type and only a single study examined a combination of three feature types. Consequently, there is limited knowledge regarding integration of multiple feature types for applications of PALSAR imagery.

Our objective is to fill this knowledge gap by assessing the potential of using various metrics of intensity, polarimetric scattering, interferometric coherence, and spatial texture extracted from multitemporal dual-polarized PALSAR data for land cover classification. Because different types of features represent different information content encapsulated in radar signals, we investigated the improvement in accuracy associated with the gain of information achieved by combining multiple feature types. Our goal is “utilitarian” in the sense that we seek to provide general guidance for practitioners related to how accuracy will be affected by combining two or more feature types. We do not delve into the mechanistic details of the classification (i.e. specific associations between features and land cover classes), but rather address the previously unanswered question of how much accuracy could potentially be improved by combining readily available multiple feature types with a commonly used classifier (random forest).

Table 1
Examples of studies using PALSAR-derived features from five major remote sensing journals.

Authors	Mode	Feature(s)				Research objective(s)	Fused with other data?
		Intensity	Polarimetric parameters	Interferometric coherence	Texture measures		
Almeida-Filho et al. (2009)	FBD	✓				Detection of new deforestation fronts	
Baghdadi et al. (2009)	FBS, FBD	✓				Harvested sugarcane monitoring	
Dong et al. (2012)	FBD	✓				Land cover mapping in tropical regions	MODIS
Dong et al. (2013)	FBD	✓				Rubber plantation mapping	Landsat TM/ETM+
Evans et al. (2010)	ScanSAR	✓				Land cover and seasonal inundation mapping	Radarsat-2
He et al. (2012)	FBD	✓				Forest stand biomass estimation	
Joyce et al. (2009)	FBS	✓		✓		Lahar path detection	
Longepe et al. (2011)	FBD	✓			✓	Regional land cover classification	
Lonnqvist et al. (2010)	FBD, PLR	✓	✓	✓		Land cover mapping	
McNairn et al. (2009)	PLR	✓	✓			Crop classification	Envisat ASAR, Radarsat-1, Landsat TM
Meyer et al. (2011)	FBS			✓		Landfast ice detection	
Santoro et al. (2009)	FBS, FBD, PLR	✓				Signature analysis of the backscatter from forests with different growth stages	
Santoro et al. (2010)	FBS, FBD	✓				Clear-cut detection	
Sun et al. (2011)	FBD, PLR	✓		✓		Forest biomass mapping	LVIS, SRTM
Tanase et al. (2010)	FBD	✓		✓		Forest burn severity estimation	
Tanase et al. (2011)	FBD, PLR	✓		✓		Forest regrowth monitoring	
Thiel et al. (2009)	FBS, FBD	✓		✓		Large-area forest monitoring	
Torbick et al. (2011)	FBS, FBD, ScanSAR	✓				Rice mapping and monitoring of hydroperiod	MODIS
Walker et al. (2010)	FBD	✓			✓	Land cover and forest mapping	SRTM
Wang and Allen (2008)	FBS	✓				Estuarine shoreline delineation	
Wang et al. (2009)	FBD	✓				Model development on rice canopy scattering	
Wolter and Townsend (2011)	FBD	✓			✓	Forest abundance estimation and forest species mapping	Radarsat-1, Landsat TM, SPOT-derived forest structure estimates
Zhang et al. (2009)	FBS	✓				Rice mapping	
Zhang et al. (2010)	FBS, FBD			✓		Seismic surface displacement analysis	

The study was conducted in Central New York State (USA), a region recognized for its significant cloudiness. Multitemporal PALSAR data provides the possibility to distinguish different land cover types based on the temporal variation of radar signals attributable mainly to the changes in physical (e.g. leaf-on and leaf-off states) and weather (e.g. freezing and precipitation) conditions, given that there has been no transition between land cover types during the considered period. The FBD mode was chosen because it contains a cross-polarized channel recording additional polarimetric data as opposed to the FBS mode. Furthermore, compared to PLR, FBD images were acquired more frequently (typically three to five times per year for most areas around the globe) in a spatially contiguous manner with a larger swath width and no gaps between the passes (Rosenqvist et al., 2007). We started by employing the four types of features individually, and then evaluated the use of all possible feature combinations. Of particular interest is the improvement in classification accuracy achieved by the feature synergies, as higher accuracy directly reflects the value of including multi-type features in land cover classification.

3. Study area and SAR data

3.1. Study area

The study area is in Central New York State, USA (Fig. 1). It lies between 42°46'41"N and 43°22'23"N latitude and 75°39'17"W and 76°35'21"W longitude with a ground extent of 66.9 km × 55.3 km (approximately 3697 km²), covering the major part of Onondaga County and a small portion of neighboring counties. Topography changes extensively in the N–S direction. The northern part is a

fairly level lake plain extending northward to Lake Ontario, while high ridges rise in the southern part extending southward to the Appalachian Plateau. The proximity to the Great Lakes results in significant cloudiness and precipitation, and heavy snowfall comes from the lake effect process and nor'easter storms. Syracuse, one of the rainiest and snowiest cities in the United States, is located at the center of the study site.

Land cover classes in the study area can be summarized into seven categories: water, barren, developed, deciduous, coniferous, shrubland, and herbaceous/planted. Definition of each class is consistent with that applied in the NLCD (National Land Cover Database) 2001 classification scheme (http://www.mrlc.gov/nlcd01_leg.php), but we placed more emphasis on woody vegetation classes to evaluate the separability of deciduous, coniferous, and shrubland using PALSAR FBD data. Since natural and semi-natural herbaceous has a minimal presence, such areas were combined with agricultural pasturelands and croplands to constitute the herbaceous/planted class. Other grass-covered land uses such as golf courses and the grass infields surrounding airport runways were labeled as developed according to the NLCD classification scheme because these are manmade structures. NLCD wetlands were grouped into one of the four vegetation classes depending on the type of vegetation cover. For example, a woody wetland pixel dominated by deciduous forest was considered deciduous in this study.

3.2. ALOS/PALSAR data

Four PALSAR scenes in the FBD mode with HH and HV polarizations were acquired over the study area on May 12, June 27, August

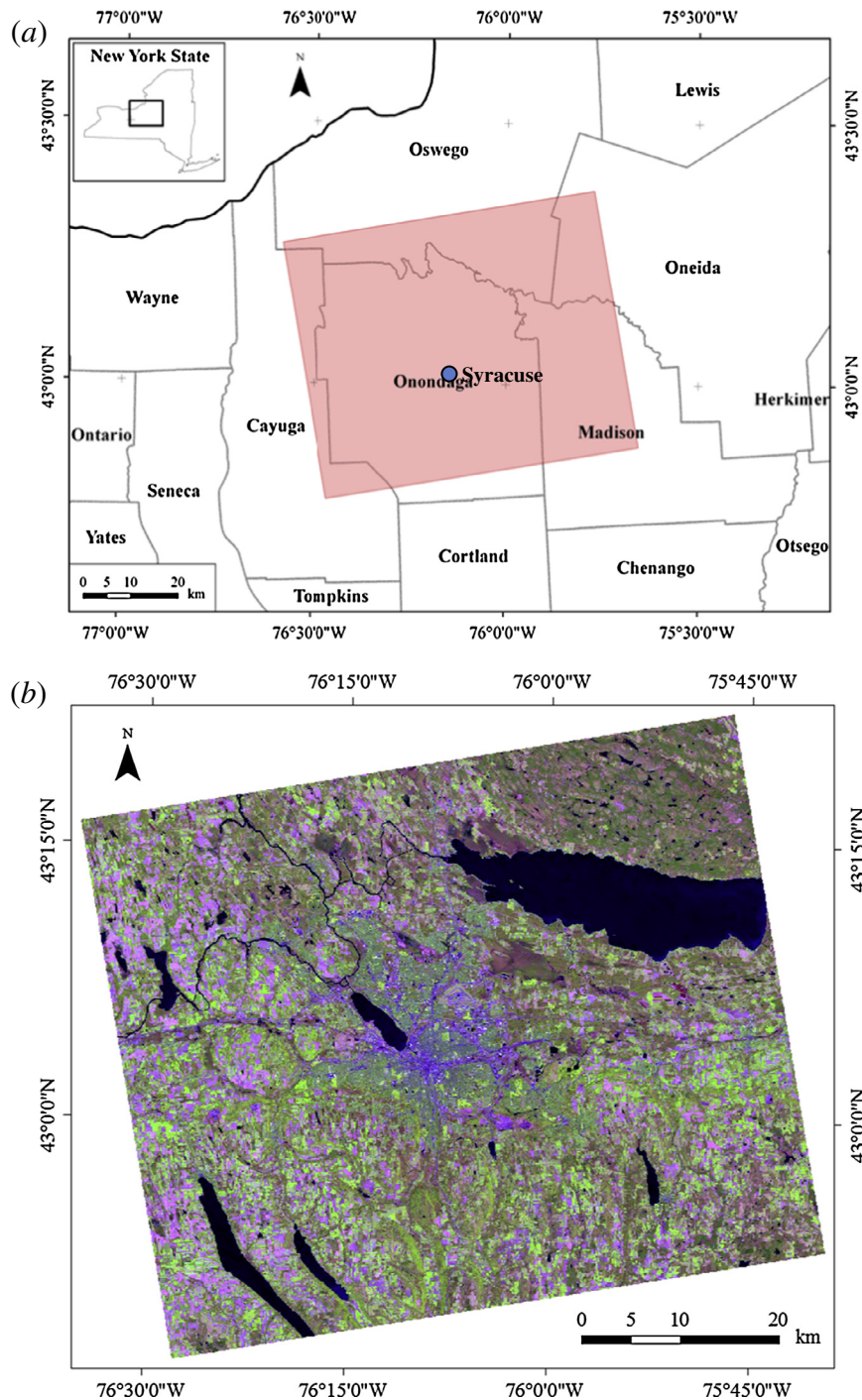


Fig. 1. (a) Location of the study area (red) in Central New York State. (b) Landsat-5 TM false-color imagery (RGB bands 5, 4, and 3) acquired over the study area on 29 April 2010, providing an overview of land cover distribution.

12, and November 12, 2010, all from an ascending orbit (path 134, frame 850) and an off-nadir angle of 34.3°. The Level 1.1 single look complex (SLC) data were ordered from the Alaska Satellite Facility (ASF) Distributed Active Archive Center (source: <https://ursa.asfdaac.alaska.edu>). Pixel spacing is 9.37 m in the slant range direction, and 3.17–3.20 m in the azimuth direction.

Meteorological data were collected at a station of NOAA’s National Climatic Data Center (NCDC) located in the City of Syracuse. Table 2 presents the daily maximum and minimum air temperatures and the cumulative precipitation within 24 h before acquisitions of PALSAR data. Most images were acquired under dry

Table 2

Meteorological conditions at the time of image acquisition.

Acquisition date	T_{max} (°C)	T_{min} (°C)	Precipitation (mm)
2010.05.12	14	3	3.6
2010.06.27	24	17	0.5
2010.08.12	31	19	0
2010.11.12	14	−1	0

Note: T_{max} and T_{min} denote the daily maximum and minimum air temperatures.

conditions. Although the precipitation event prior to the May acquisition may impact the discrimination of vegetation classes due to a higher moisture content in the canopy and soil, the effect

was considered marginal in this study since the precipitation was relatively light (less than 4 mm). The minimum air temperature for the November scene was around the freezing point, but confirmed by the MODIS daily 250 m surface reflectance product (MOD09GQ), there was no snow on the ground or ice on the water over the study area at the date of acquisition. The first recorded snowfall in the winter of 2010 occurred in early December.

4. Methods

Fig. 2 illustrates the procedure adopted in this study. Multiple types of features were first extracted from the PALSAR images. Pixel-based classification was then performed on different combinations of the features using a training sample collected from high

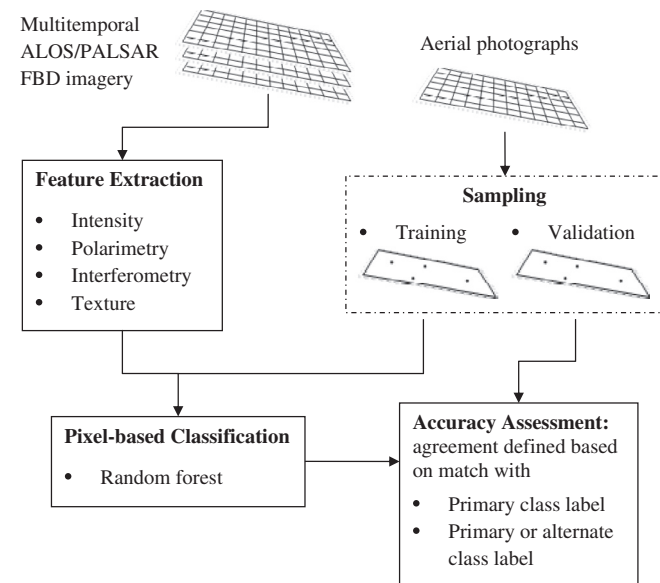


Fig. 2. Flow chart of the experimental procedure.

resolution aerial photographs. Results were compared with the validation data on a pixel-by-pixel basis to quantitatively assess classification performance for different definitions of agreement. Detailed descriptions are provided in the following sections.

4.1. Data processing and feature extraction

A total of 132 features were extracted for the subsequent classification (Table 3), and they are grouped into four major feature types: intensity (16), polarimetry (8), interferometry (12) and texture (96). All features were orthorectified and filtered using the Next ESA SAR Toolbox (NEST, <http://nest.array.ca>), an open-source implementation developed by Array (Toronto, ON, Canada) under contract to the European Space Agency (ESA). Here, we used Shuttle Radar Topographic Mission (SRTM, <http://srtm.usgs.gov/>) 30 m (i.e. 1 arc second) digital elevation model (DEM) for the orthorectification, and all features were converted to WGS-84 datum and UTM Zone 18 North coordinate system and resampled to 30 m pixel size through a bilinear interpolation. A 5×5 Enhanced Lee filter was also applied to reduce speckle noise while preserving detailed spatial information (Lopes et al., 1990). Examples of these features are shown in Fig. 3, one from each feature type. These features together provide the maximum discriminative power of the data set to separate different land cover types defined in this study.

4.1.1. Intensity

The backscattering coefficient, also known as the normalized radar cross section (σ^0 , in decibels (dB)), is the most commonly used statistic in applications of PALSAR imagery. The conversion between the complex data and σ^0 was given by Shimada et al. (2009),

$$\sigma^0 = 10 \log_{10} (I^2 + Q^2) + CF - A \quad (1)$$

where I and Q are the real and imaginary parts of the SLC product at Level 1.1. CF is the calibration factor distributed around the value of -83.0 dB, with a standard deviation of 0.76 dB. The conversion factor A is 32.0 , which is a theoretically derived value. σ^0 characterizes the strength (or intensity) of the pulses returned and detected by

Table 3

Summary of features extracted from PALSAR FBD data. Abbreviation explanations are provided in the text.

Category	Variable	Data	Number of layers			
Intensity	σ_{HH}^0	May 12, June 27, August 12, November 12	16 (4×4)			
	σ_{HV}^0					
	$\sigma_{HH}^0 - \sigma_{HV}^0$					
	$\sigma_{HH}^0 / \sigma_{HV}^0$					
Polarimetry ^a	H	May 12, June 27, August 12, November 12	8 (2×4)			
	α					
Interferometry		Image pair	Δt (days)	B_{\parallel}^b (m)	B_{\perp}^c (m)	12 (2×6)
		May 12 vs. June 27	46	220	158	
	γ_{HH}	May 12 vs. August 12	92	493	641	
	γ_{HV}	May 12 vs. November 12	184	381	529	
		June 27 vs. August 12	46	273	484	
		June 27 vs. November 12	138	161	371	
		August 12 vs. November 12	92	112	113	
Texture	ENE	$\sigma_{HH}^0, \sigma_{HV}^0$ on May 12, June 27, August 12, November 12	96 ($6 \times 2 \times 4 \times 2^d$)			
	CON					
	DIS					
	HOM					
	ENT					
	COR					

^a Polarimetric parameters H and α were derived based on dual-polarized data.

^b Parallel baseline.

^c Perpendicular baseline.

^d Two window sizes were used for texture computation.

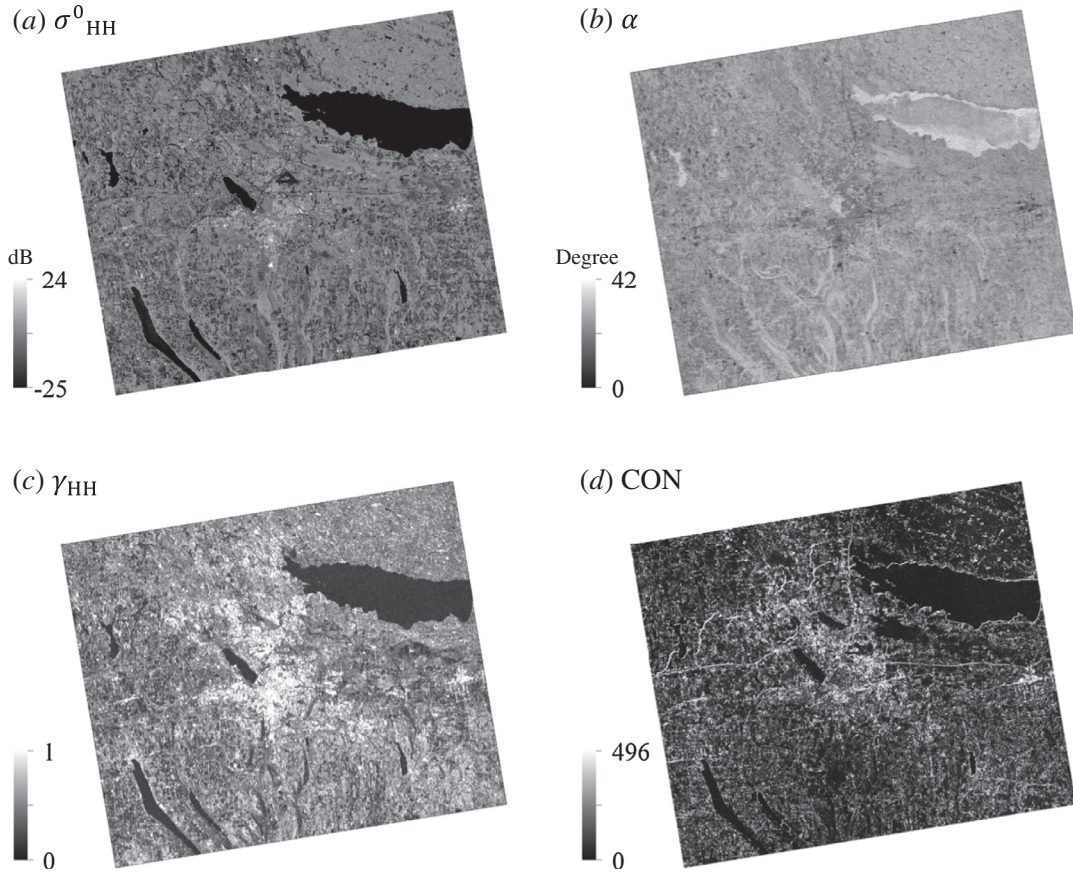


Fig. 3. Examples of the features used in this study. (a) HH backscattering coefficient at August 12, (b) alpha at August 12, (c) coherence at HH between August 12 and November 12, and (d) the GLCM contrast computed on (a) using a 3 by 3 moving window.

the antenna, so it is a fundamental indicator of ground conditions, particularly of vegetation growth.

For each PALSAR data set used in this study, both HH and HV backscattering coefficients, as well as the difference and ratio between the two polarization bands, were computed as the intensity feature listed in Table 3.

4.1.2. Polarimetric decomposition parameters

Since the FBD mode of the PALSAR sensor employs a single transmit polarization of H and dual coherent reception of H and V, the decomposition approach especially designed for coherent dual-polarimetric data, namely H/α or entropy/alpha decomposition (Cloude, 2007), was conducted to provide additional information on scattering mechanisms (i.e. surface, volume and double bounce scattering).

Two statistical parameters of entropy (H) and alpha (α) were calculated on the basis of an orthogonal eigenvector decomposition of the 2×2 complex covariance matrix constructed using measurements of radar polarimetry HH and HV at each pixel, and

$$H = -\sum_{i=1}^2 P_i \log_2 P_i, \quad P_i = \lambda_i / \sum_{i=1}^2 \lambda_i \quad (2)$$

$$\alpha = \sum_{i=1}^2 P_i \alpha_i, \quad \sum_{i=1}^2 \alpha_i = \pi/2 \quad (3)$$

where P_i is the probability of the normalized eigenvalue λ_i quantifying the relative contribution with respect to the total backscatter power, and α_i is determined from the i th eigenvector representing the type of scattering.

The physical interpretation of the two polarimetric parameters defined in Eqs. (2) and (3) can be found in some previous studies (e.g. Lopez-Sanchez et al., 2011, 2012). Entropy (H) is a measure of the randomness of a scatterer. Low entropy suggests that the pixel is dominated by a single scattering type, and for high entropy more than one scattering process is involved. Alpha (α) is crucial for identifying the dominant scattering mechanism. It has a range of 0–90 degrees corresponding to a continuous change from surface scattering (e.g. open areas), moving to dipole or volume scattering (e.g. forest canopy), and finally reaching double bounce scattering (e.g. buildings).

In this study, H/α decomposition was performed on each PALSAR data set using the PolSARpro software package (Pottier et al., 2009) distributed by ESA. Therefore, four pairs of entropy and alpha parameters were extracted as the polarimetric feature.

4.1.3. Interferometric coherence

SAR interferometry is a technique for combining two complex SAR images over the target area acquired at different times from a nearly repeating orbit (Zebker and Villasenor, 1992), and it has been widely applied to retrieve complementary information relative to the information contained in individual images (e.g. Smith and Askne, 2001; Engdahl et al., 2001; Blaes and Defourny, 2003; Meyer et al., 2011). The interferometric coherence γ is defined as,

$$\gamma = \frac{|E\{Z_1 Z_2^*\}|}{\sqrt{E\{|Z_1|^2\} E\{|Z_2|^2\}}} \quad (4)$$

where Z_1 and Z_2 represents the master and slave image, respectively, $*$ denotes the complex conjugate, and $|\cdot|$ the magnitude and

$E\{\cdot\}$ the expectation operator. In practice, the maximum likelihood estimator (MLE) of coherence, $\hat{\gamma}$, was found by replacing expectation values with averages (Seymour and Cumming, 1994),

$$\hat{\gamma}_{ij} = \frac{|\sum_N Z_1 Z_2^*|}{\sqrt{\sum_N |Z_1|^2 \sum_N |Z_2|^2}} \quad (5)$$

where summation is calculated over a window of N pixels centered at (i, j) . The selection of window size is always a compromise between spatial resolution and precision of coherence estimation (Engdahl et al., 2001). Large window sizes could produce coherence with small bias and standard deviation (Bamler and Hartl, 1998), but also smooth out details on the resulting coherence maps through spatial averaging.

The value of coherence varies between 0 (incoherence) and 1 (perfect coherence), quantifying the degree of similarity of two co-registered images taken from slightly different look angles (Hanssen, 2001). According to Zebker and Villasenor (1992), coherence is affected by a number of factors related to the signal-to-noise ratio (SNR), image geometry, spatial baseline, and temporal interval between the two image acquisitions. In a repeat-pass scenario, however, temporal changes and volume scattering are two most important causes of decorrelation, especially in vegetated areas over the growing season (Hyypä et al., 2000; Engdahl et al., 2001; Wagner et al., 2003). Variations of the environmental conditions, such as wind, precipitation and freeze events, are also sources of temporal decorrelation (Koskinen et al., 2001; Santoro et al., 2002; Askne et al., 2003; Pulliainen et al., 2003; Thiel and Schmullius, 2013). Usually, croplands and forests lose coherence rapidly due to vegetation growth and changes in the arrangement of scatterers (e.g. leaves), whereas in urban/built-up areas coherence remains high even between image pairs separated by a long time interval.

The interferometric processing of the PALSAR data was performed in the NEST environment. All the four images were co-registered at sub-pixel accuracy into a common geometry by maximizing local spatial correlation between master and slave images at a series of small square areas spread throughout the images. Coherence, at both HH and HV polarizations, was then estimated from every pair of the original SLC images using a moving window of 5 by 25 pixels (in range and azimuth direction, respectively), corresponding to about 75 m in both across- and along-track (see descriptions of pixel spacing and off-nadir angle in Section 3.2). Consequently, 12 interferometric coherence images were generated, six at each polarization for all possible combinations of the four scenes selected.

4.1.4. Texture measures

Haralick et al. (1973) introduced a general procedure for extracting textural information in the spatial domain from the gray-level co-occurrence matrix (GLCM). The derived statistical features have been effectively utilized in many SAR applications, such as forest biomass estimation (e.g. Kuplich et al., 2005), land cover assessment (e.g. van der Sanden and Hoekman, 1999; Longepe et al., 2011; Qi et al., 2012), and sea ice classification (e.g. Barber and LeDrew, 1991; Baraldi and Parmiggiani, 1995; Soh and Tsatsoulis, 1999; Clausi, 2002).

The GLCM outlines the distance and angular spatial relationship between pixels within the moving window. For an image initially quantized to N_g gray levels, the matrix consists of $N_g \times N_g$ elements, each representing the joint probability of occurrence $p(i, j)$ of pairs of pixels with gray levels i and j separated by a given distance (d) and direction (θ) in a specific window. Practically, smaller values of N_g may accelerate the calculation, but this is usually associated with the loss of information as quantization essentially smoothes an image. Therefore, we used a reasonably fine scheme

with 64 gray levels to preserve detailed information while avoiding high computational load. To keep the size of textural feature space manageable, only two window sizes were tested, one at a smaller scale of 90 m (i.e. 3 pixels) and the other at a larger scale of 450 m (i.e. 15 pixels). Moreover, inter-pixel distance was fixed at one ($d = 1$) since most relevant correlation exists between adjacent pixels (van de Wouwer et al., 1999), and omnidirectional features were obtained by averaging out the results in the four directions of $\theta = 0, 45, 90$ and 135 degrees.

For a given window size, six second-order GLCM-based texture measures, including energy (ENE), contrast (CON), dissimilarity (DIS), homogeneity (HOM), entropy (ENT) and correlation (COR), were extracted from every quantized layer of HH and HV backscattering coefficients, and they are defined as

$$\text{ENE} = \sum_{i=1}^{N_g} \sum_{j=1}^{N_g} p^2(i, j) \quad (6)$$

$$\text{CON} = \sum_{i=1}^{N_g} \sum_{j=1}^{N_g} p(i, j) (i - j)^2 \quad (7)$$

$$\text{DIS} = \sum_{i=1}^{N_g} \sum_{j=1}^{N_g} p(i, j) |i - j| \quad (8)$$

$$\text{HOM} = \sum_{i=1}^{N_g} \sum_{j=1}^{N_g} \frac{p(i, j)}{1 + (i - j)^2} \quad (9)$$

$$\text{ENT} = - \sum_{i=1}^{N_g} \sum_{j=1}^{N_g} p(i, j) \ln p(i, j) \quad (10)$$

$$\text{COR} = \sum_{i=1}^{N_g} \sum_{j=1}^{N_g} p(i, j) \frac{(i - \mu_x)(j - \mu_y)}{\sigma_x \sigma_y} \quad (11)$$

where μ_x , μ_y , σ_x , and σ_y are the means and standard deviations for the row- and column-marginal probabilities of the co-occurrence matrix composed of $p(i, j)$, and

$$\mu_x = \sum_{i=1}^{N_g} \sum_{j=1}^{N_g} ip(i, j)$$

$$\mu_y = \sum_{i=1}^{N_g} \sum_{j=1}^{N_g} jp(i, j) \quad (12)$$

$$\sigma_x = \sqrt{\sum_{i=1}^{N_g} \sum_{j=1}^{N_g} (i - \mu_x)^2 p(i, j)}$$

$$\sigma_y = \sqrt{\sum_{i=1}^{N_g} \sum_{j=1}^{N_g} (j - \mu_y)^2 p(i, j)} \quad (13)$$

The various features we selected characterize spatial information from different aspects. Energy, also known as uniformity or angular second moment, is a measure of the smoothness of an image. The smoother the image, the higher will be the value of energy. Contrast measures the amount of local variations, and a smaller value corresponds to a lower degree of variation. Dissimilarity and homogeneity are another two features to represent image contrast. Entropy is an indication of the complexity or the randomness. A more informative image with complex spatial structure usually results in a higher entropy value. Correlation

describes the linear dependency of gray levels of the neighboring pixels, and it has lower values for an image with uncorrelated pixels, such as the noise.

4.2. Sampling and response designs for training and validation

Reference (or ground) data for both training and validation were collected by visual interpretation of 1 ft and 2 ft resolution aerial photography produced by the New York Statewide Digital Orthoimagery Program (NYSDOP, <http://gis.ny.gov/gateway/ortho-program/>) between 2008 and 2011. All orthoimagery contained four bands (blue, green, red and infrared), capable of both natural color and color infrared display. A pixel with a size of 30 m × 30 m consistent with processed PALSAR data was chosen as the sampling unit. To capture the unique signature of each land cover class, only pure pixels were sampled as training data, with the exception of some sample pixels in the developed class that cover a mixture of constructed materials and vegetation on the ground (e.g. in residential areas).

The selection of validation data followed a probability sampling design to ensure that statistically rigorous design-based inference can be established for estimating accuracy of the entire region from a sample (Stehman, 2000). Stratified random sampling was implemented to specify the locations at which validation data would be obtained. Preliminary analysis showed that the percentage of pixels mapped as barren, water, and coniferous was around 0.1%, 7%, and 8%, respectively, whereas the other four classes (i.e. developed, deciduous, shrubland, and herbaceous/planted) were more common with greater than 15% coverage. Each of the three rare classes was defined as a stratum to allow for increasing the sample size in each class and thereby reducing the standard error of estimated user's accuracy. In contrast, the four common classes were combined as a single stratum to limit the total number of strata. To avoid tailoring the strata to just one of the maps, we defined the strata using four of the classified maps. The four maps were selected to include one map from the set of maps of each number of feature types (e.g. the map with all four feature types, one of the maps with three feature types, etc.). To create the stratification, pixels labeled as barren by any of the four classified maps were first assigned to stratum I. Then a pixel was assigned to stratum II if any map labeled that pixel as water (unless the pixel was already in stratum I in which case it stayed as stratum I). Similarly, stratum III was defined based on the coniferous class with the exclusion of pixels in strata I and II. All the remaining pixels constituted the common class stratum IV. A sample of 100 pixels was selected from each of stratum I, II and III, and 500 sample pixels were selected from stratum IV. Simple random sampling was used to select the sample pixels within each stratum. The sampling design was equal probability for pixels within a stratum, but pixels from different strata had different probabilities of being included in the sample.

Due to the common existence of mixed pixels and the uncertainty in identifying reference class labels based on photo interpretation (as opposed to field observation), it is not always possible to unambiguously assign a single, crisp cover type to the sampling unit (Stehman and Czaplewski, 1998). Therefore, we determined the dominant or most likely (i.e. primary) land cover class for each pixel in the validation sample set, and also had the option of providing one alternate reference class label. For example, if a sample pixel was located on the boundary of a parking lot adjacent to deciduous forest that has limited coverage inside of the pixel, the primary and alternate labels would be developed and deciduous, respectively. This labeling protocol provides insight into the potential impact of reference data quality on the assessment and interpretation of classification accuracy (Stehman and Foody, 2009).

Table 4
Sample sets for training and validation.

Class	Training	Validation	
		Total (on the primary reference class label)	Number (and percentage) of pixels with an alternate reference class label
Water	240	106	3 (3%)
Barren	219	35	5 (14%)
Developed	1481	126	30 (24%)
Deciduous	653	202	94 (47%)
Coniferous	439	57	35 (61%)
Shrubland	759	66	45 (68%)
Herbaceous/Planted	1209	208	67 (32%)
Total	5000	800	279 (35%)

Table 4 summarizes the composition of training and validation sets. In total, 5000 pixels constituted the training data and an additional 800 pixels were collected for accuracy assessment. Approximately 35% of the validation sample included an alternate class label, of which most had mixed land cover due to the difference in spatial resolution of the 30 m × 30 m map versus 1 ft × 1 ft (~0.3 m) and 2 ft × 2 ft (~0.6 m) reference data.

4.3. Pixel-based classification

This study opted for an ensemble learning algorithm named random forest (RF) (Breiman, 2001) to classify different land cover types using PALSAR-derived features. During the training process, RF creates a large number of unpruned Classification and Regression Trees (CART), each from a bootstrapped sample of approximately two thirds of the original data and considering only a random subset of the input features at each splitting node. The output of the algorithm is determined by aggregating the predictions from all constructed trees (i.e. majority votes for classification, average for regression). Moreover, an assessment of the importance of each feature can be performed on the out-of-bag samples – the one third data that are excluded from the training sample for a particular tree – by randomly permuting all the values of one feature while keeping the rest unchanged. This is to mimic the absence of that feature from the model, and a high prediction accuracy decrease averaged over all the trees indicates a significant contribution of that feature to the classification/regression task.

Similar to a single decision tree (DT), RF does not require any implicit assumption on data distribution, and is capable of accommodating different types or scales of input data. However, RF is superior to DT because it runs more efficiently on high-dimensional data sets, and it does not overfit showing greater resistance to outliers (or noise) in the training sample (Breiman, 2001; Pal and Mather, 2003). The random selection of variables for a split at each node also minimizes the impact of correlated variables compared to the use of a single tree. All these characteristics make RF attractive in remote sensing classification studies, and it has been successfully applied to multispectral (e.g. Pal, 2005; Timm and McGarigal, 2012), hyperspectral (e.g. Ham et al., 2005; Lawrence et al., 2006), SAR (e.g. Waske and Braun, 2009), and LiDAR data (e.g. Martinuzzi et al., 2009), or multisource data sets (e.g. Gislason et al., 2006; Waske and Benediktsson, 2007; Guo et al., 2011).

Fifteen RF models were developed using the same training sample but different combinations of features consisting of one, two, three or four feature types. In each model, 500 classification trees were constructed, and the number of features randomly chosen at each node was set to the square root of the number of inputs. Consequently, fifteen classified maps were produced, one from each model. For details of feature combination in each classification scenario, the reader is referred to Table 5.

Table 5
Estimated accuracy (%) for classifications using different combinations of feature types where agreement is defined as a match between the map class and either the primary or alternate reference label of the sample pixel (“*PriAlt*”). Producer’s accuracy (PA) and user’s accuracy (UA) are presented as deviations from the results of the classifier using four types of features. Standard errors of estimated overall accuracy were smaller than 2% in all scenarios.

Feature combination ^a				Estimated accuracy (%)															
INT	POL	COH	TEX	Overall accuracy	Deciduous		Coniferous		Shrubland		Herbaceous/Planted		Developed		Barren		Water		
					PA	UA	PA	UA	PA	UA	PA	UA	PA	UA	PA	UA	PA	UA	
<i>Four feature type scenario</i>																			
✓	✓	✓	✓	72	66	93	77	67	71	50	64	93	88	50	7	77	90	99	
<i>Three feature type scenarios</i>																			
✓	✓	✓		71	2	0	-3	3	2	3	-4	0	-3	-5	2	-32	0	-1	
✓	✓		✓	70	2	-3	-3	1	-3	-3	-3	-4	-3	0	-1	-6	-2	0	
✓		✓	✓	68	-3	-5	-17	-12	-10	-8	-3	-4	-2	-3	-6	23	-1	0	
	✓	✓	✓	66	-7	-1	-21	-3	-5	-7	-3	-9	-2	-5	-1	0	-2	-1	
<i>Two feature type scenarios</i>																			
✓	✓			69	3	-5	-5	-3	-3	2	-6	-2	-6	-6	-6	-55	1	0	
✓		✓		69	4	-3	-10	-1	-4	-2	-6	-3	-7	-6	0	-55	-3	0	
✓			✓	67	-1	-7	-18	-7	-16	-13	-4	-4	-3	-4	-6	23	-3	0	
		✓	✓	65	-4	-6	-37	-2	-9	-11	-6	-14	0	-3	-3	-5	-6	1	
	✓		✓	63	-9	-12	-37	-13	-15	-9	-4	-15	-1	-4	-5	23	-6	-3	
	✓	✓		62	-18	-12	-23	-1	-5	-10	-3	-8	-7	-9	1	-10	-1	-1	
<i>One feature type scenarios</i>																			
✓				65	1	-8	-18	-5	-4	-5	-14	-4	-5	-8	-6	-67	-2	0	
			✓	62	-12	-11	-52	-19	-28	-15	-3	-26	3	-2	-6	3	-8	-1	
		✓		57	-20	-18	-47	-16	-7	-16	-11	-18	-6	-9	-2	-2	-9	1	
	✓			56	-22	-21	-35	-24	-22	-15	-3	-26	-15	-8	-6	3	-13	-4	

^a INT, POL, COH, and TEX denote intensity, polarimetric parameters, interferometric coherence, and texture measures, respectively.

4.4. Accuracy assessment

Assessing classification accuracy evaluates the degree to which a map agrees with the reference data. In this study, a sample-based accuracy assessment was conducted inferring accuracy estimates from a sample to the population. We defined two types of agreement to compute accuracy estimates, one being a match between the map class of the sample pixel and the primary reference label only (denoted as “*PriOnly*”), and the other being a match between the map class and either the primary or alternate reference label (denoted as “*PriAlt*”). Using both the primary and alternate labels in the matching protocol can accommodate thematic ambiguity of the reference data (Olofsson et al., 2014). Accuracy estimates derived from the *PriAlt* definition of agreement will be higher than the corresponding estimates based on the *PriOnly* definition.

An error matrix approach (Story and Congalton, 1986) was adopted to describe classification accuracy and characterize errors. Cell proportions of the error matrix and the associated accuracy measures were estimated from the validation sample following standard probability sampling protocols to construct statistically consistent accuracy estimates. The four strata we established for selecting the validation sample do not correspond exactly to the map classes of any classification performed, so the accuracy estimators applicable to this situation described by Stehman (2014) were used. Overall accuracy and class-specific producer’s and user’s accuracies and their accompanying standard errors were computed for both definitions of agreement *PriOnly* and *PriAlt* and each of the fifteen classified maps using the 800 sample pixels selected for validation. Computations were conducted using Mathwork’s MATLAB software (Natick, MA, USA).

5. Results

5.1. Accuracy of classifications derived from different feature types

The inclusion of an alternate label in the definition of agreement generally improved the overall accuracy by 8–10% in all fifteen scenarios relative to defining agreement as a match between the map

label and the primary reference label only. This is consistent with the general expectation that using only the primary label may underestimate classification accuracy, as *PriOnly* is a very strict definition of agreement permitting no allowance for ambiguity in the reference land cover label. The relative performance of the different combinations of feature types remains fundamentally the same for the *PriAlt* and *PriOnly* definitions of agreement, so the subsequent description of results mainly focuses on the *PriAlt* estimates (Table 5). The four groups of scenarios correspond respectively to the total number of feature types implemented. Within each group results are sorted by overall accuracy in descending order. To facilitate the identification of more considerable differences, producer’s accuracy (PA) and user’s accuracy (UA) are presented as deviations from the results of the most accurate classifier which is the classifier using all four feature types. Accuracies estimated by *PriOnly* are provided in the table of Appendix A, arranged in the same order as Table 5.

In general, the overall accuracy was gradually improved as more feature types were used for classification. For example, the exclusive use of intensity was capable of classifying different land cover types to an overall accuracy of 65%. The inclusion of polarimetric scattering parameters increased overall accuracy to 69%, which was further improved to 71% by combining interferometric coherence also. Another 1% improvement was achieved with the final incorporation of texture measures, leading to the highest overall accuracy of 72%. The classified map created using all four feature types is presented in Fig. 4.

Differences in accuracy were more substantial for certain classes with respect to the number of feature types used for classification. Particularly, both producer’s and user’s accuracies of the four vegetation classes decreased extensively in the one type classifiers compared to the scenario employing all types of features simultaneously. In contrast, feature type synergies had relatively marginal effect on the estimated accuracies of developed and water. Unlike the moderate accuracy of the developed class, water was consistently well classified in most scenarios with producer’s accuracy of 81–91% and user’s accuracy above 95%.

Among the four feature types, intensity was the most indispensable because all classifications with the highest overall accuracy in

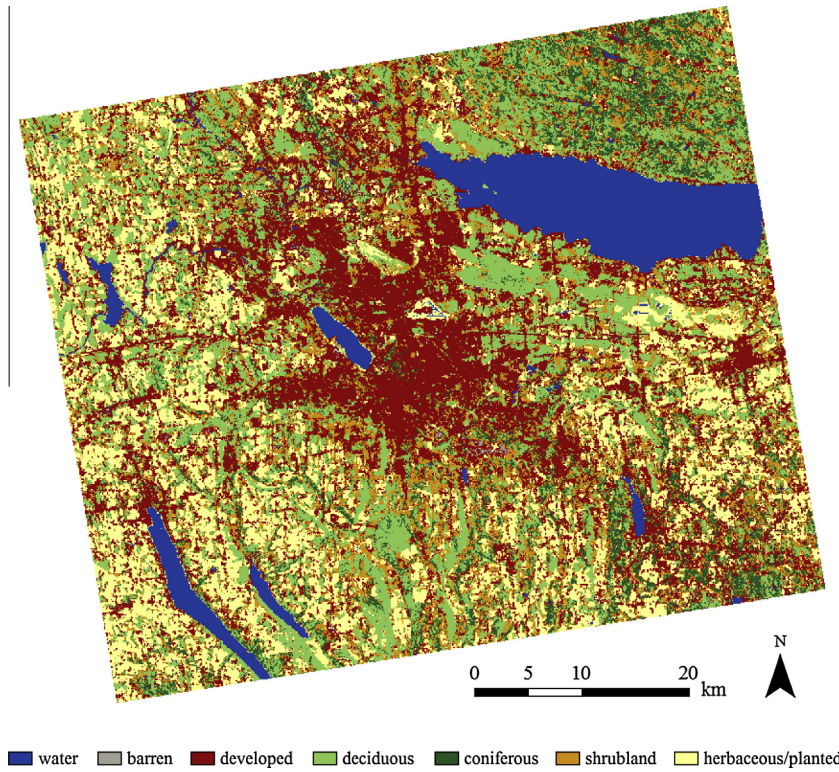


Fig. 4. Land cover map created using all four feature types described in this study (overall accuracy is 72%).

Table 6

Error matrix and accuracy estimates (%) based on the “*PriAlt*” definition of agreement for the classification using only the intensity metrics (16 inputs). Producer’s accuracy (PA) and user’s accuracy (UA) are reported with standard errors (SE) in parentheses. Overall accuracy is 65% with a SE of 2%.

Class	Water	Barren	Developed	Deciduous	Coniferous	Shrubland	Herbaceous/Planted	Total	UA (SE)
Water	7.551	0.000	0.078	0.000	0.000	0.000	0.000	7.629	99 (1)
Barren	0.003	0.010	0.025	0.003	0.000	0.003	0.054	0.099	10 (5)
Developed	0.236	0.193	12.981	3.796	1.442	1.867	10.927	31.442	41 (3)
Deciduous	0.316	0.319	0.609	19.512	0.860	0.790	0.761	23.168	84 (3)
Coniferous	0.000	0.000	0.258	2.189	4.636	0.258	0.129	7.469	62 (6)
Shrubland	0.000	0.326	0.951	3.764	0.890	6.483	2.054	14.468	45 (5)
Herbaceous/Planted	0.477	0.032	0.812	0.000	0.000	0.316	14.088	15.725	90 (3)
Total	8.584	0.879	15.715	29.264	7.828	9.717	28.013	100	
PA (SE)	88 (4)	1 (1)	83 (4)	67 (3)	59 (6)	67 (6)	50 (4)		

Table 7

Error matrix and accuracy estimates (%) based on the “*PriAlt*” definition of agreement for the classification using all features of intensity, polarimetry, interferometry and texture (132 inputs). Producer’s accuracy (PA) and user’s accuracy (UA) are reported with standard errors (SE) in parentheses. Overall accuracy is 72% with a SE of 2%.

Class	Water	Barren	Developed	Deciduous	Coniferous	Shrubland	Herbaceous/Planted	Total	UA (SE)
Water	7.551	0.000	0.078	0.000	0.000	0.000	0.000	7.629	99 (1)
Barren	0.000	0.064	0.013	0.003	0.000	0.000	0.003	0.083	77 (8)
Developed	0.552	0.342	13.954	3.138	0.790	2.690	6.679	28.144	50 (4)
Deciduous	0.316	0.000	0.000	18.063	0.158	0.000	0.948	19.486	93 (2)
Coniferous	0.000	0.000	0.258	2.318	6.439	0.515	0.129	9.658	67 (5)
Shrubland	0.000	0.474	0.632	3.764	0.948	8.040	2.213	16.071	50 (5)
Herbaceous/Planted	0.003	0.000	0.948	0.158	0.000	0.158	17.662	18.929	93 (2)
Total	8.423	0.879	15.883	27.444	8.335	11.403	27.633	100	
PA (SE)	90 (4)	7 (3)	88 (3)	66 (4)	77 (5)	71 (5)	64 (4)		

each group incorporated intensity metrics. Using features of polarimetric scattering and interferometric coherence individually resulted in lower overall accuracies relative to the use of intensity or texture measures. However, greater improvement was achieved when polarimetric and interferometric types of features were combined with intensity, suggesting that both are capable of adding

useful thematic information complementary to intensity metrics. Conversely, when combined with intensity, texture metrics resulted in limited improvement over using intensity alone, and this two feature type combination of intensity and texture had inferior accuracy to other two feature type scenarios that combined intensity with scattering and intensity with coherence.

The highest classification accuracy was achieved by integrating multiple feature types. It requires more time and effort to extract features of polarimetric scattering, interferometric coherence and spatial texture than would be the case of using intensity metrics only. The value added by each feature type in terms of classification accuracy varied by land cover class. Therefore, benefits and costs of incorporating different types of features should be evaluated depending on the specific land cover class of interest for an intended application. For example, shrubland producer's and user's accuracies were highest when texture measures were not combined with the other three feature types, suggesting that spatial information contributed little to the enhanced separability of shrubland from other land cover types and thus texture was not necessarily needed for the shrubland classification.

5.2. Detailed assessment of selected classifications

Tables 6 and 7 summarize the estimated error matrices based on the *PriAlt* agreement definition for the two classified maps created using intensity alone and all four types of features, respectively. For each matrix, reference class labels form the columns and map class labels form the rows. Cell entries are expressed as percent area of the region. Main diagonal entries (displayed in bold) represent correct classifications, and off-diagonal entries identify errors.

A high proportion of disagreement occurred between the developed and herbaceous/planted classes, especially for the map created using intensity metrics only. Substantial misclassification of herbaceous/planted pixels to the developed class resulted in remarkably high developed commission error and high herbaceous/planted omission error. This may be attributable to the difficulties in distinguishing grass-dominated areas in the developed context (e.g. golf courses) from natural and semi-natural grassland, pasture, and cropland that were defined as herbaceous/planted in this study. However, the inclusion of interferometric, polarimetric and textural features partially resolved this problem, giving rise to a 14% increase in producer's accuracy of herbaceous/planted, and a 9% increase in user's accuracy of developed. Similarly, a substantial proportion of the barren omission error is because it was labeled as developed or shrubland. Deciduous was also a relatively large contributor to the barren omission error when intensity was used exclusively. Nonetheless, barren is a very rare class on the landscape representing less than 0.1% of the study area from the map perspective, and therefore had little impact on the overall quality of the classification.

6. Discussion

To further investigate the contribution of each feature to the overall classification, an assessment of feature importance was implemented on the classifier using all four feature types. The contribution was quantified by the mean decrease in accuracy given the absence of the feature evaluated (Fig. 5). Features of intensity, polarimetric scattering and interferometric coherence contributed more than the numerous texture measures, as randomly permuting values of any texture measure resulted in a marginally decreased accuracy by less than 1%. This is consistent with the accuracy estimates presented in Table 5. Because intensity metrics represent the strength of the returned signals after interacting with ground objects, polarimetric parameters characterize the type and contribution of scattering mechanisms and interferometric coherence indicates the degree to which surfaces remain unchanged, these three feature types were more informative and of greater importance in radar applications relative to texture measures when used in combination.

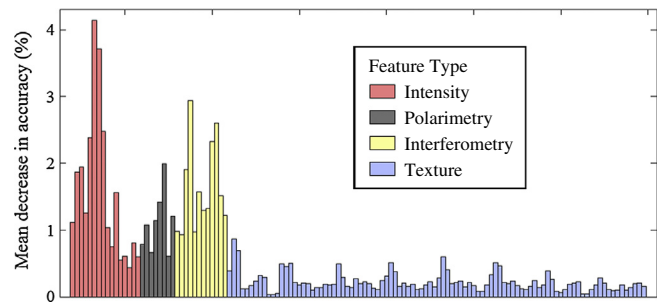


Fig. 5. Feature importance in terms of mean decrease in accuracy.

For the intensity metrics, the backscattering coefficients at the HV polarization (intensities 5–8) are more important compared to HH backscatters (intensities 1–4). Because cross-polarized radar returns are attributable to multiple volume scattering from within the vegetation canopy, HV polarization presents stronger sensitivity to vegetation structure and biomass (Le Toan et al., 1992; McNairn et al., 2009; Wolter and Townsend, 2011). Consequently, it is more critical for vegetation discrimination in this study as vegetation has majority coverage over the study area. In contrast, combining intensity metrics of difference (intensities 9–12) and ratio (intensities 13–16) calculated from the corresponding HH and HV backscatters yielded limited improvement in classification accuracy.

The measure of feature importance provides some guidance to the potential selection of most important features for classification. Determining *a priori* the combinations of features that contain more separable land cover information can reduce the number of inputs to the classification algorithm and therefore accelerate the classification process. To examine whether this is practically viable and how accuracy would be affected, we selected the four most important metrics of each feature type using the information presented in Fig. 5. Those metrics in the best set of feature combinations within each group of scenarios presented in Table 5 were then used as classification inputs. Overall accuracies estimated by the *PriAlt* definition of agreement are summarized in Table 8. For every combination set, accuracy increased as the number of metrics of each feature type increased. The rate of improvement in accuracy as metrics were added was greatest for the scenarios using intensity and intensity combined with polarimetric scattering parameters. For all feature type combinations, using all the metrics available improved overall accuracy compared to using only the best four metrics of each feature type. Although computing efficiency was not an issue in our study, applications addressing larger areas may benefit from preliminary analyses of feature importance that would reduce the dimensionality of input features with limited loss of information.

As a data exploration step before the classification, a separability analysis on each of the four feature types can facilitate understanding how well each feature type separates the classes of interest when used in isolation (see Appendix B). Information obtained from the separability analysis Appendix B table is analogous to what an error matrix delivers, quantifying the potential of two classes being confused with each other. Consistent with accuracies of the single feature type scenarios (Table 5), intensity and texture were the two types that showed stronger capability in distinguishing classes. However, these individual separability analyses do not appear informative regarding the performance of feature type combinations. For example, while intensity and texture produced as single feature types the greatest separability of classes, the best (i.e. most accurate) two- and three-feature type combinations did not include both intensity and texture feature types.

Table 8

Overall accuracy (%) based on the “PriAlt” definition of agreement for classifications using the most important metrics of each feature type in the best set of feature combinations identified from Table 5.

Feature combination ^a				Overall accuracy (%)				
INT	POL	COH	TEX	Best 1 metric	Best 2 metrics	Best 3 metrics	Best 4 metrics	All metrics
✓				38	52	56	58	65
✓	✓			52	61	64	66	69
✓	✓	✓		59	63	67	68	71
✓	✓	✓	✓	61	65	68	68	72

^a INT, POL, COH, and TEX denote intensity, polarimetric parameters, interferometric coherence, and texture measures, respectively.

A variety of avenues for future research emerged during this study. In our study, seven major classes from the NLCD 2001 classification scheme were assessed and provided a generally accepted level of detail of land cover land use information. Training the algorithm on more detailed class levels (e.g. different agricultural crops) might be a way of fine tuning the classifier to take further advantage of PALSAR capabilities.

Because of limited availability of PALSAR imagery and reference data, our comparison of combinations of feature types focused on a single site. Case study investigations remain the norm in remote sensing practice as demonstrated by the fact that 19 of the 24 articles cited in Table 1 also used one site. Although methods for designing multi-site studies to yield more statistically representative conclusions have been proposed (e.g. Stehman, 2006), our case study results contribute, in conjunction with the Table 1 studies, to the understanding of the impact of feature types on accuracy of land cover classifications. Qualitatively similar results would be expected for other sites as all seven classes of interest assessed in this study are typical land cover types and all four feature types were solely derived from PALSAR Level 1.1 SLC data. However, the degree to which accuracy is improved by combining multi-type features is likely dependent on each specific application. Therefore, the evaluation of feature type combinations should be extended to additional sites to better characterize the differences in accuracy to be expected in different settings.

The joint use of Landsat imagery and PALSAR-derived multi-type features in land cover classification is also worth investigating. Because optical data capture spectral characteristics and radar data record scattering characteristics of each land cover class, the union of these data sources is anticipated to yield more substantial and accurate thematic information than is possible from using each source in isolation. With the successful launch of Landsat 8 (Landsat Data Continuity Mission, LDCM) and ALOS-2/PALSAR-2, integrating all features of intensity, polarimetric scattering, interferometric coherence and spatial texture with Landsat imagery will provide a methodological basis for future studies using Landsat 8 and PALSAR-2.

7. Conclusions

The synergistic use of different types of features extracted from multitemporal dual-polarized ALOS/PALSAR imagery for land cover classification was evaluated in this study. Different combinations of metric groups representing intensity, polarimetric scattering, interferometric coherence, and spatial texture were used as classification inputs. Our hypothesis investigated whether the gain of information content by combining multiple feature types improved classification accuracy. Results showed that polarimetric, interferometric and textural features contributed beneficial

Table A.1

Estimated accuracy (%) for classifications using different combinations of feature types where agreement is defined as a match between the map class and the primary reference label of the sample pixel (“PriOnly”). Producer’s accuracy (PA) and user’s accuracy (UA) are presented as deviations from the results of the classifier using four types of features. Standard error of overall accuracy is smaller than 2% in all scenarios. Rows of the table are ordered as in Table 5.

Feature combination ^a				Estimated accuracy (%)															
INT	POL	COH	TEX	Overall accuracy	Deciduous		Coniferous		Shrubland		Herbaceous/Planted		Developed		Barren		Water		
					PA	UA	PA	UA	PA	UA	PA	UA	PA	UA	PA	UA	PA	UA	
<i>Four feature type scenario</i>																			
✓	✓	✓	✓	62	55	83	54	44	56	34	59	88	82	43	7	77	88	99	
<i>Three feature type scenarios</i>																			
✓	✓	✓		61	1	-2	-2	0	3	4	-4	-1	-4	-4	2	-34	0	-1	
✓	✓	✓	✓	62	2	-1	-1	2	-2	0	-2	-4	-2	-1	-1	-6	0	0	
✓	✓	✓		59	0	-10	-18	-1	-11	-5	-3	-4	-2	-3	-6	23	1	0	
✓	✓	✓	✓	57	-6	-4	-17	3	-6	-4	-3	-10	-2	-5	-1	-4	-2	-1	
<i>Two feature type scenarios</i>																			
✓	✓			59	3	-10	-10	-3	-5	2	-7	-1	-7	-6	-6	-55	1	0	
✓	✓	✓		59	4	-3	-6	0	-3	-1	-7	-4	-8	-5	0	-56	-1	0	
✓		✓	✓	58	0	-12	-18	2	-17	-8	-3	-4	-3	-5	-6	23	-1	0	
	✓	✓	✓	56	-4	-8	-34	-6	-9	-6	-6	-16	4	-2	-3	-10	-6	1	
	✓	✓	✓	55	-6	-15	-28	2	-15	-4	-5	-14	2	-5	-5	23	-5	-3	
	✓	✓		53	-17	-14	-19	-7	-6	-8	-3	-10	-10	-7	0	-13	-1	-1	
<i>One feature type scenarios</i>																			
✓				56	0	-13	-18	-6	-8	-1	-13	-5	-5	-7	-6	-67	0	0	
		✓		53	-9	-16	-39	-5	-25	-6	-3	-28	8	-3	-6	3	-8	-1	
		✓	✓	49	-17	-19	-33	-8	-3	-10	-11	-21	-9	-7	-2	-7	-7	1	
	✓			47	-21	-25	-30	-20	-25	-14	-5	-26	-15	-7	-6	3	-11	-4	

^a INT, POL, COH, and TEX respectively denote intensity, polarimetric parameters, interferometric coherence, and texture measures.

Table B.1

Separability of the seven classes assessed on each of the four feature types. Separability is represented by the Jeffries-Matusita (JM) distance (Richards and Jia, 1999). The values range from 0 to 2, indicating how well the two classes are statistically separate. Higher values suggest better separability.

	Water	Barren	Developed	Deciduous	Coniferous	Shrubland
<i>(a) Intensity metrics^a</i>						
Barren	1.51					
Developed	1.61	0.46				
Deciduous	1.98	1.39	1.23			
Coniferous	1.98	1.50	1.37	0.41		
Shrubland	1.91	0.98	0.93	0.50	0.66	
Herbaceous/Planted	1.58	1.31	1.43	1.92	1.94	1.77
<i>(b) Polarimetric scattering parameters</i>						
Barren	1.49					
Developed	1.56	0.45				
Deciduous	1.24	0.90	0.86			
Coniferous	1.29	0.86	0.82	0.08		
Shrubland	1.24	0.57	0.65	0.24	0.23	
Herbaceous/Planted	1.26	0.76	0.95	1.29	1.31	1.01
<i>(c) Interferometric coherence</i>						
Barren	1.82					
Developed	1.71	0.63				
Deciduous	1.58	1.23	0.94			
Coniferous	1.71	1.33	0.87	0.58		
Shrubland	1.57	1.18	0.69	0.58	0.45	
Herbaceous/Planted	1.43	1.45	1.34	1.05	1.37	1.20
<i>(d) Texture measures^a</i>						
Barren	2.00					
Developed	2.00	1.45				
Deciduous	1.99	1.99	1.97			
Coniferous	2.00	1.99	1.95	1.14		
Shrubland	2.00	1.97	1.91	1.19	1.00	
Herbaceous/Planted	1.99	1.96	1.91	1.34	1.50	0.90

^a Some of the metrics were removed to avoid the singular matrix and inversion problem during the analysis.

thematic information when combined with the intensity metrics, providing more pronounced discriminative capability among different land cover types, in particular the multiple vegetation classes assessed in our study. The integration of all feature types improved overall accuracy to 72%, an increase of 7% relative to using just intensity. More considerable improvement was observed for producer's accuracy and user's accuracy of the vegetation classes. As further applications of PALSAR imagery emerge, our study serves as a reference guide on how to extract and combine multi-type features with key references and processing steps.

Acknowledgements

This work was supported through NASA's Biodiversity Program (grant # NNX09AK16G) to H. Jin and G. Mountrakis and NASA's Carbon Monitoring Systems Program (grant # NNX13AP48G) to S. Stehman. We thank the two anonymous reviewers for their careful review and many constructive comments that led to improvements in the manuscript.

Appendix A

See Table A.1.

Appendix B

See Table B.1.

References

Almeida-Filho, R., Shimabukuro, Y.E., Rosenqvist, A., Sanchez, G.A., 2009. Using dual-polarized ALOS PALSAR data for detecting new fronts of deforestation in the Brazilian Amazonia. *Int. J. Remote Sens.* 30, 3735–3743.

- Askne, J., Santoro, M., Smith, G., Fransson, J.E.S., 2003. Multitemporal repeat-pass SAR interferometry of boreal forests. *IEEE Trans. Geosci. Remote Sens.* 41, 1540–1550.
- Baghdadi, N., Boyer, N., Todoroff, P., Hajji, M.E., Begue, A., 2009. Potential of SAR sensors TerraSAR-X, ASAR/ENVISAT and PALSAR/ALOS for monitoring sugarcane crops on reunion island. *Remote Sens. Environ.* 113, 1724–1738.
- Bamler, R., Hartl, P., 1998. Synthetic aperture radar interferometry. *Inverse Prob.* 14, 1–54.
- Baraldi, A., Parmiggiani, F., 1995. An investigation of the textural characteristic associated with gray level cooccurrence matrix statistical parameters. *IEEE Trans. Geosci. Remote Sens.* 33, 293–304.
- Barber, D.G., LeDrew, E.F., 1991. SAR sea ice discrimination using texture statistics: a multivariate approach. *Photogram. Eng. Remote Sens.* 57, 385–395.
- Blaes, X., Defourny, P., 2003. Retrieving crop parameters based on tandem ERS 1/2 interferometric coherence images. *Remote Sens. Environ.* 88, 374–385.
- Breiman, L., 2001. Random forests. *Mach. Learn.* 45, 5–32.
- Clausi, D.A., 2002. An analysis of co-occurrence texture statistics as a function of grey level quantization. *Can. J. Remote Sens.* 28, 45–62.
- Cloude, S.R., 2007. The dual polarization entropy/alpha decomposition: a PALSAR case study. In: *Proceedings of the 3rd International Workshop on Science and Applications of SAR Polarimetry and Polarimetric Interferometry*, Frascati, Italy, January 22–26, CD-ROM. European Space Agency, Noordwijk, Netherlands, p. 6.
- Danklmayer, A., Doring, B.J., Schwerdt, M., Chandra, M., 2009. Assessment of atmospheric propagation effects in SAR images. *IEEE Trans. Geosci. Remote Sens.* 47, 3507–3518.
- Dong, J., Xiao, X., Chen, B., Torbick, N., Jin, C., Zhang, G., Biradar, C., 2013. Mapping deciduous rubber plantations through integration of PALSAR and multi-temporal landsat imagery. *Remote Sens. Environ.* 134, 392–402.
- Dong, J., Xiao, X., Sheldon, S., Biradar, C., Xie, G., 2012. Mapping tropical forests and rubber plantations in complex landscapes by integrating PALSAR and MODIS imagery. *ISPRS J. Photogram. Remote Sens.* 74, 20–33.
- Engdahl, M.E., Borgeaud, M., Rast, M., 2001. The use of ERS-1/2 tandem interferometric coherence in the estimation of agricultural crop heights. *IEEE Trans. Geosci. Remote Sens.* 39, 1799–1806.
- Evans, T.L., Costa, M., Telmer, K., Silva, T.S.F., 2010. Using ALOS/PALSAR and RADARSAT-2 to map land cover and seasonal inundation in the Brazilian Pantanal. *IEEE J. Select. Top. Appl. Earth Observ. Remote Sens.* 3, 560–575.
- Friedl, M.A., McIver, D.K., Hodges, J.C.F., Zhang, X.Y., Muchoney, D., Strahler, A.H., Woodcock, C.E., Gopal, S., Schneider, A., Cooper, A., Baccini, A., Gao, F., Schaaf, C., 2002. Global land cover mapping from MODIS: algorithms and early results. *Remote Sens. Environ.* 83, 287–302.
- Fung, A.K., 1994. *Microwave Scattering and Emission Models and Their Applications*. Artech House, Boston, MA.

- Gislason, P.O., Benediktsson, J.A., Sveinsson, J.R., 2006. Random forests for land cover classification. *Pattern Recogn. Lett.* 27, 294–300.
- Guo, L., Chehata, N., Mallet, C., Boukir, S., 2011. Relevance of airborne lidar and multispectral image data for urban scene classification using random forests. *ISPRS J. Photogram. Remote Sens.* 66, 56–66.
- Ham, J., Chen, Y., Crawford, M.M., Ghosh, J., 2005. Investigation of the random forest framework for classification of hyperspectral data. *IEEE Trans. Geosci. Remote Sens.* 43, 492–501.
- Hansen, M.C., DeFries, R.S., Townshend, J.R.G., Sohlberg, R., 2000. Global land cover classification at 1 km spatial resolution using a classification tree approach. *Int. J. Remote Sens.* 21, 1331–1364.
- Hansen, R.F., 2001. *Radar Interferometry: Data Interpretation and Error Analysis*. Kluwer Academic Publishers.
- Haralick, R.M., Shanmugam, K., Dinstein, I., 1973. Textural features for image classification. *IEEE Trans. Syst. Man Cyber.* 3, 610–621.
- He, Q., Cao, C., Chen, E., Sun, G., Ling, F., Pang, Y., Zhang, H., Ni, W., Xu, M., Li, Z., Li, X., 2012. Forest stand biomass estimation using ALOS PALSAR data based on LiDAR-derived prior knowledge in the Qilian mountain, Western China. *Int. J. Remote Sens.* 33, 710–729.
- Homer, C., Huang, C., Yang, L., Wylie, B.K., Coan, M., 2004. Development of a 2001 national land-cover database for the United States. *Photogram. Eng. Remote Sens.* 70, 829–840.
- Homer, C., Dewitz, J., Fry, J., Coan, M., Hossain, N., Larson, C., Herold, N., McKerrow, A., VanDriel, J.N., Wickham, J., 2007. Completion of the 2001 national land cover database for the conterminous United States. *Photogram. Eng. Remote Sens.* 73, 337–341.
- Hoen, E.W., Zebker, H., 2000. Penetration depths inferred from interferometric volume decorrelation observed over the greenland ice sheet. *IEEE Trans. Geosci. Remote Sens.* 38, 2571–2583.
- Hyyppä, J., Hyyppä, H., Inkinen, M., Engdahl, M., Linko, S., Zhu, Y., 2000. Accuracy comparison of various remote sensing data sources in the retrieval of forest stand attributes. *For. Ecol. Manage.* 128, 109–120.
- JAXA (Japan Aerospace Exploration Agency), 2014. *Advanced Land Observing Satellite-2 "DAICHI-2" (ALOS-2)*. <<http://global.jaxa.jp/projects/sat/alos2/index.html>> (accessed 02.08.14).
- Joyce, K.E., Samsonov, S., Manville, V., Jongens, R., Graettinger, A., Cronin, S.J., 2009. Remote sensing data types and techniques for lahar path detection: a case study at Mt Ruapehu, New Zealand. *Remote Sens. Environ.* 113, 1778–1786.
- Koskinen, J.T., Pulliainen, J.T., Hyyppä, J.M., Engdahl, M.E., Hallikainen, M.T., 2001. The seasonal behavior of interferometric coherence in boreal forest. *IEEE Trans. Geosci. Remote Sens.* 39, 820–829.
- Kuplich, T.M., Curran, P.J., Atkinson, P.M., 2005. Relating SAR image texture to the biomass of regenerating tropical forest. *Int. J. Remote Sens.* 26, 4829–4854.
- Lawrence, R.L., Wood, S.D., Sheley, R.L., 2006. Mapping invasive plants using hyperspectral imagery and breiman cutler classifications (RandomForest). *Remote Sens. Environ.* 100, 356–362.
- Le Toan, T., Beaudoin, A., Riou, J., Guyon, D., 1992. Relating forest biomass to SAR data. *IEEE Trans. Geosci. Remote Sens.* 30, 403–411.
- Longepe, N., Rakwatin, P., Isoguchi, O., Shimada, M., Uryu, Y., Yulianto, K., 2011. Assessment of ALOS PALSAR 50 m Orthorectified FBD Data for Regional Land Cover Classification by Support Vector Machines. *IEEE Trans. Geosci. Remote Sens.* 49, 2135–2150.
- Lonnqvist, A., Rauste, Y., Molinier, M., Hame, T., 2010. Polarimetric SAR data in land cover mapping in boreal zone. *IEEE Trans. Geosci. Remote Sens.* 48, 3652–3662.
- Lopes, A., Touzi, R., Nezry, E., 1990. Adaptive speckle filters and scene heterogeneity. *IEEE Trans. Geosci. Remote Sens.* 28, 992–1000.
- Lopez-Sanchez, J.M., Ballester-Berman, J.D., Hajnsek, I., 2011. First results of rice monitoring practices in Spain by means of time series of TerraSAR-X Dual-Pol images. *IEEE J. Sel. Top. Appl. Earth Observ. Remote Sens.* 4, 412–422.
- Lopez-Sanchez, J.M., Cloude, S.R., Ballester-Berman, J.D., 2012. Rice phenology monitoring by means of SAR polarimetry at X-band. *IEEE Trans. Geosci. Remote Sens.* 50, 2695–2709.
- Martinuzzi, S., Vierling, L.A., Gould, W.A., Falkowski, M.J., Evans, J.S., Hudak, A.T., Vierling, K.T., 2009. Mapping snags and understory shrubs for a LiDAR-based assessment of wildlife habitat suitability. *Remote Sens. Environ.* 113, 2533–2546.
- McNairn, H., Shang, J., Jiao, X., Champagne, C., 2009. The contribution of ALOS PALSAR multipolarization and polarimetric data to crop classification. *IEEE Trans. Geosci. Remote Sens.* 47, 3981–3992.
- Meyer, F.J., Mahoney, A.R., Eicken, H., Denny, C.L., Druckenmiller, H.C., Hendricks, S., 2011. Mapping arctic landfast ice extent using L-band synthetic aperture radar interferometry. *Remote Sens. Environ.* 115, 3029–3043.
- Miettinen, J., Liew, S.C., 2011. Separability of insular Southeast Asian woody plantation species in the 50 m resolution ALOS PALSAR mosaic product. *Remote Sens. Lett.* 2, 299–307.
- Olofsson, P., Foody, G.M., Herold, M., Stehman, S.V., Woodcock, C.E., Wulder, M.A., 2014. Good practices for estimating area and assessing accuracy of land change. *Remote Sens. Environ.* 148, 42–57.
- Pal, M., 2005. Random forest classifier for remote sensing classification. *Int. J. Remote Sens.* 26, 217–222.
- Pal, M., Mather, P.M., 2003. An assessment of the effectiveness of decision tree methods for land cover classification. *Remote Sens. Environ.* 86, 554–565.
- Pohl, C., van Genderen, J.L., 1998. Multisensor image fusion in remote sensing: concepts, methods and applications. *Int. J. Remote Sens.* 19, 823–854.
- Pottier, E., Ferro-Famil, L., Allain, S., Cloude, S.R., Hajnsek, I., Papathanassiou, K., Moreira, A., Williams, M., Minchella, A., Lavallo, M., Desnos, Y.-L., 2009. Overview of the PolSARpro V4.0 software: the open source toolbox for polarimetric and interferometric polarimetric SAR data processing. In: *Proceedings of 2009 IEEE International Geoscience and Remote Sensing Symposium*, Cape Town, South Africa, July 12–17, vol. 4, pp. 936–939.
- Pulliaainen, J., Engdahl, M., Hallikainen, M., 2003. Feasibility of multi-temporal interferometric SAR data for stand-level estimation of boreal forest stem volume. *Remote Sens. Environ.* 85, 397–409.
- Qi, Z., Yeh, A.G., Li, X., Lin, Z., 2012. A novel algorithm for land use and land cover classification using RADARSAT-2 polarimetric SAR data. *Remote Sens. Environ.* 118, 21–39.
- Rauste, Y., 2005. Multi-temporal JERS SAR data in boreal forest biomass mapping. *Remote Sens. Environ.* 97, 263–275.
- Richards, J.A., Jia, X., 1999. *Remote Sensing Digital Image Analysis: An Introduction*. Springer-Verlag, Berlin.
- Rignot, E., Echelmeyer, K., Krabill, W., 2001. Penetration depth of interferometric synthetic-aperture radar signals in snow and ice. *Geophys. Res. Lett.* 28, 3501–3504.
- Rosenqvist, A., Shimada, M., Ito, N., Watanabe, M., 2007. ALOS PALSAR: a pathfinder mission for global-scale monitoring of the environment. *IEEE Trans. Geosci. Remote Sens.* 45, 3307–3316.
- Santoro, M., Askne, J., Smith, G., Fransson, J.E.S., 2002. Stem volume retrieval in boreal forests from ERS-1/2 interferometry. *Remote Sens. Environ.* 81, 19–35.
- Santoro, M., Fransson, J.E.S., Eriksson, L.E.B., Ulander, L.M.H., 2010. Clear-cut detection in swedish boreal forest using multi-temporal ALOS PALSAR backscatter data. *IEEE J. Sel. Top. Appl. Earth Observ. Remote Sens.* 3, 618–631.
- Santoro, M., Fransson, J.E.S., Eriksson, L.E.B., Magnusson, M., Ulander, L.M.H., Olsson, H., 2009. Signatures of ALOS PALSAR L-band Backscatter in Swedish Forest. *IEEE Trans. Geosci. Remote Sens.* 47, 4001–4019.
- Santoro, M., Eriksson, L., Askne, J., Schmillius, C., 2006. Assessment of stand-wise stem volume retrieval in boreal forest from JERS-1 L-band SAR backscatter. *Int. J. Remote Sens.* 27, 3425–3454.
- Seymour, M.S., Cumming, I.G., 1994. Maximum likelihood estimation for SAR interferometry. In: *Proceedings of the 1994 IEEE International Geosciences and Remote Sensing Symposium*, Pasadena, CA, August 8–12, vol. 4, pp. 2272–2275.
- Shimada, M., Isoguchi, O., Tadono, T., Isono, K., 2009. PALSAR radiometric and geometric calibration. *IEEE Trans. Geosci. Remote Sens.* 47, 3915–3932.
- Simard, M., Saatchi, S.S., De Grandi, G., 2000. The use of decision tree and multiscale texture for classification of JERS-1 SAR data over tropical forest. *IEEE Trans. Geosci. Remote Sens.* 38, 2310–2321.
- Smith, G., Askne, J., 2001. Clear-CUT DETECTION USING ERS interferometry. *Int. J. Remote Sens.* 22, 3651–3664.
- Soh, L., Tsatsoulis, C., 1999. Texture analysis of SAR sea ice imagery using gray level co-occurrence matrices. *IEEE Trans. Geosci. Remote Sens.* 37, 780–795.
- Stehman, S.V., 2000. Practical implications of design-based sampling inference for thematic map accuracy assessment. *Remote Sens. Environ.* 72, 35–45.
- Stehman, S.V., 2006. Design, analysis, and inference for studies comparing thematic accuracy of classified remotely sensed data: a special case of map comparison. *J. Geogr. Syst.* 8, 209–226.
- Stehman, S.V., 2014. Estimating area and map accuracy for stratified random sampling when the strata are different from the map classes. *Int. J. Remote Sens.* 35, 4923–4939.
- Stehman, S.V., Foody, G.M., 2009. Accuracy assessment. In: Warner, T.A., Nellis, M.D., Foody, G.M. (Eds.), *The SAGE Handbook of Remote Sensing*. Sage Publications, London, pp. 297–309.
- Stehman, S.V., Czaplewski, R.L., 1998. Design and analysis for thematic map accuracy assessment: fundamental principles. *Remote Sens. Environ.* 64, 331–344.
- Story, M., Congalton, R.G., 1986. Accuracy assessment: a user's perspective. *Photogram. Eng. Remote Sens.* 52, 397–399.
- Sun, G., Ranson, K.J., Guo, Z., Zhang, Z., Montesano, P., Kimes, D., 2011. Forest biomass mapping from lidar and radar synergies. *Remote Sens. Environ.* 115, 2906–2916.
- Tanase, M.A., Santoro, M., Wegmuller, U., de la Riva, J., Perez-Cabello, F., 2010. Properties of X-, C- and L-band repeat-pass interferometric SAR coherence in mediterranean pine forests affected by fires. *Remote Sens. Environ.* 114, 2182–2194.
- Tanase, M., de la Riva, J., Santoro, M., Perez-Cabello, F., Kasischke, E., 2011. Sensitivity of SAR data to post-fire forest regrowth in mediterranean and boreal forests. *Remote Sens. Environ.* 115, 2075–2085.
- Thiel, C.J., Thiel, C., Schmillius, C.C., 2009. Operational large-area forest monitoring in siberia using ALOS PALSAR summer intensities and winter coherence. *IEEE Trans. Geosci. Remote Sens.* 47, 3993–4000.
- Thiel, C., Schmillius, C., 2013. Investigating ALOS PALSAR interferometric coherence in central Siberia at unfrozen and frozen conditions: implications for forest growing stock volume estimation. *Can. J. Remote Sens.* 39, 232–250.
- Timm, B.C., McGarigal, K., 2012. Fine-scale remotely-sensed cover mapping of coastal dune and salt marsh ecosystems at cape cod national seashore using random forests. *Remote Sens. Environ.* 127, 106–117.
- Torbick, N., Salas, W.A., Hagen, S., Xiao, X., 2011. Monitoring rice agriculture in the sacramento valley, USA with multitemporal PALSAR and MODIS imagery. *IEEE J. Sel. Top. Appl. Earth Observ. Remote Sens.* 4, 451–457.
- Ulaby, F.T., Moore, R.K., Fung, A.K., 1986. *Microwave Remote Sensing: Active and Passive*, Volume 3, From Theory to Applications. Artech House, Norwood, MA.

- van de Wouwer, G., Scheunders, P., van Dyck, D., 1999. Statistical texture characterization from discrete wavelet representations. *IEEE Trans. Image Process.* 8, 592–598.
- van der Sanden, J.J., Hoekman, D.H., 1999. Potential of airborne radar to support the assessment of land cover in a tropical rain forest environment. *Remote Sens. Environ.* 68, 26–40.
- Wagner, W., Luckman, A., Vietmeier, J., Tansey, K., Balzter, H., Schmullius, C., Davidson, M., Gaveau, D., Gluck, M., Toan, T.L., Quegan, S., Shvidenko, A., Wiesmann, A., Yu, J.J., 2003. Large-scale mapping of boreal forest in SIBERIA using ERS tandem coherence and JERS backscatter data. *Remote Sens. Environ.* 85, 125–144.
- Walker, W.S., Stickler, C.M., Kellndorfer, J.M., Kirsch, K.M., Nepstad, D.C., 2010. Large-area classification and mapping of forest and land cover in the Brazilian Amazon: a comparative analysis of ALOS/PALSAR and landsat data sources. *IEEE J. Select. Top. Appl. Earth Observ. Remote Sens.* 3, 594–604.
- Wang, C., Wu, J., Zhang, Y., Pan, G., Qi, J., Salas, W.A., 2009. Characterizing L-band Scattering of paddy rice in southeast China with radiative transfer model and multitemporal ALOS/PALSAR imagery. *IEEE Trans. Geosci. Remote Sens.* 47, 988–998.
- Wang, Y., Allen, T.R., 2008. Estuarine shoreline change detection using Japanese ALOS PALSAR HH and JERS-1 L-HH SAR data in the Albemarle-Pamlico Sounds, North Carolina, USA. *Int. J. Remote Sens.* 29, 4429–4442.
- Waske, B., Benediktsson, J.A., 2007. Fusion of support vector machines for classification of multisensor data. *IEEE Trans. Geosci. Remote Sens.* 45, 3858–3866.
- Waske, B., Braun, M., 2009. Classifier ensembles for land cover mapping using multitemporal SAR imagery. *ISPRS J. Photogram. Remote Sens.* 64, 450–457.
- Wolter, P.T., Townsend, P.A., 2011. Multi-sensor data fusion for estimating forest species composition and abundance in northern minnesota. *Remote Sens. Environ.* 115, 671–691.
- Zebker, H.A., Villasenor, J., 1992. Decorrelation in interferometric radar echoes. *IEEE Trans. Geosci. Remote Sens.* 30, 950–959.
- Zhang, K., Ng, A.H., Ge, L., Dong, Y., Rizos, C., 2010. Multi-Path PALSAR interferometric observations of the 2008 magnitude 8.0 Wenchuan earthquake. *Int. J. Remote Sens.* 31, 3449–3463.
- Zhang, Y., Wang, C., Wu, J., Qi, J., Salas, W.A., 2009. Mapping paddy rice with multitemporal ALOS/PALSAR imagery in Southeast China. *Int. J. Remote Sens.* 30, 6301–6315.